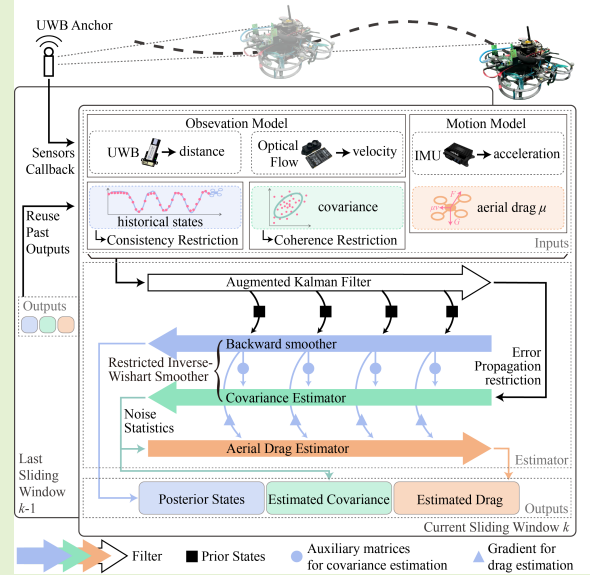


An Adaptive Sliding Window Estimator for Positioning of Unmanned Aerial Vehicle Using a Single Anchor

Kaiwen Xiong, Sijia Chen, Wei Dong

Abstract—Localization using a single range anchor combined with onboard optical-inertial odometry offers a lightweight solution that provides multidimensional measurements for the positioning of unmanned aerial vehicles. Unfortunately, the performance of such lightweight sensors varies with the dynamic environment, and the fidelity of the dynamic model is also severely affected by environmental aerial flow. To address this challenge, we propose an adaptive sliding window estimator equipped with an estimation reliability evaluator, where the states, noise covariance matrices and aerial drag are estimated simultaneously. The aerial drag effects are first evaluated based on posterior states and covariance. Then, an augmented Kalman filter is designed to pre-process multidimensional measurements and inherit historical information. Subsequently, an inverse-Wishart smoother is employed to estimate posterior states and covariance matrices. To further suppress potential divergence, a reliability evaluator is devised to infer estimation errors. We further determine the fidelity of each sensor based on the error propagation. Extensive experiments are conducted in both standard and harsh environments, demonstrating the adaptability and robustness of the proposed method. The root mean square error reaches 0.15 m, outperforming the state-of-the-art approach.

Index Terms—Position Estimation, Single Anchor, Adaptive Noise Covariance, Aerial Drag Estimation



I. INTRODUCTION

UNMANNED aerial vehicles (UAVs) are increasingly employed to replace manpower in harsh environments [1]. To achieve autonomous execution and efficient operation, high-precision positioning and navigation of UAVs are urgently demanded [2]. Unfortunately, in challenging scenarios such as cave exploration [3], facilities maintenance [4], environmental interference and rapid changes underscore the need for further refinement of positioning methods.

Typically, to achieve high-precision positioning, many works leverage peripheral equipment, including GNSS [5], [6], motion capture system [7], pre-established beacon system [8] and assistant robot [9]. However, GNSS navigation often becomes infeasible due to signal obstruction, as highlighted by several studies [10], while deploying additional peripheral equipment may be limited by resource constraints in

numerous applications. Hence, onboard sensors have garnered significant interest. Two primary categories include visual odometry (VO), which encompasses cameras [11], [12] and lidar [13], albeit requiring substantial computational resources. The alternative category comprises non-visual methods such as ultra-wideband radio (UWB) [14], inertial measurement units (IMU), or a combination of both [15], which are lightweight but usually have limited information and inadequate positioning precision in complex situations. Under this premise, integrated systems like UWB-VO [16], visual-inertial odometry [17], and vision-IMU-UWB odometry [18], [19] effectively mitigate drawbacks from both categories. To handle environmental interference and achieve better positioning precision, it is critical to distinguish varying degrees of sensor failure and properly exploit return data according to sensor fidelity.

Adaptive algorithms are developed to tackle this problem. They concurrently estimate states and noise's statistical properties based on optimal estimators. Among various methods, one category is empirical adjustment incorporating deliberately designed factors [20] and fuzzy system [21]. The other category explores statistical approaches such as exploiting moment estimation of sample covariance [22], [23] and special prior

This work was supported in part by Shanghai Jiaotong University, Shanghai, China.

Kaiwen Xiong, Sijia Chen and Wei Dong are with the State Key Laboratory of Mechanical System and Vibration, School of Mechanical Engineering, Shanghai Jiaotong University, Shanghai, 200240, China. Corresponding author: Wei Dong, E-mail: dr.dongwei@sjtu.edu.cn.

distributions [24], [25]. The methods above demonstrate their competence in slowly changing environments. However, in harsh scenarios, current estimators struggle to assess estimation errors synchronously, rendering them susceptible to faulty data due to interference. Furthermore, these estimators can hardly adapt to sudden environmental changes, which increases the risk of potential divergence, underscoring the urgent need for more robust solutions.

Moreover, the variation in aerial drag presents another facet of environmental change. Accounting for aerial drag is crucial in the motion modeling of UAVs [26], significantly enhancing the precision of position estimation [27]. Many studies have studied the estimation of aerial drag coefficients [28]–[30], but due to the complexity of aerodynamics and limited computational resources, more efficient methods are deserved in practical application.

To address the above problems, we elaborately develop a novel method called *restricted adaptive sliding window estimator (RASWE)*, which simultaneously operates state estimation, covariance matrix adaptation, and aerial drag adjustment. Considering sensor configuration, an optical flow sensor and IMU are employed to compensate for the limited operation range and single data dimension of UWB. Then, the dynamics are reformulated considering aerial drag effects. An augmented Kalman filter pre-processes all data from the sensor system and reuses historical output states under coherence restriction. The processed data are sent to the backward smoother, yielding posterior states utilized to estimate noise covariance matrices under the control of error propagation restriction. A cost function is formulated based on the idea that the dynamic model with proper aerial drag matrix derives the prior state that approaches the posterior state, which helps to adjust the aerial drag matrix via gradient descent. All outputs within one sliding window are reused as inputs at the next timestep. Finally, experiments are conducted in both common and harsh environments to demonstrate the adaptability of the proposed method. Additionally, we design various ablation experiments to validate the effectiveness of each design.

The major contributions of our work are threefold: 1) We propose an augmented Kalman filter to estimate the position of UAV using a single anchor efficiently. 2) We elaborately design an error propagation matrix as an online error inspector to assess estimation performance and develop a restricted inverse-Wishart smoother to derive posterior states and adjust noise covariance synchronously. 3) We formulate a cost function based on the idea that the prior state obtained by dynamics should approach the posterior state, and we construct a novel aerial drag estimator via the gradient descent method to enhance estimation performance.

II. PRELIMINARIES

A. Notations

In this article, an m by n matrix, $\mathbf{A} \in \mathbb{R}^{m \times n}$, is referred to by capital bold letter, whereas vector of dimension n , $\mathbf{x} \in \mathbb{R}^n$, is denoted by a lowercase bold letter. Identity and zero matrix of dimension $m \times n$ are represented as $\mathbf{I}_{m \times n}$ and $\mathbf{0}_{m \times n}$ respectively, and to simplify, the square ones of size n are abbreviated as \mathbf{I}_n and $\mathbf{0}_n$ respectively. If their dimension is

not emphasized, the index will be omitted. The transposition and inverse of matrix (\cdot) are $(\cdot)^T$ and $(\cdot)^{-1}$ respectively. Also, prior and posterior quantities usually are decorated with superscripts, $(\cdot)^{\check{}}$ and $(\cdot)^{\hat{}}$ respectively. Commonly, a quantity with index, $(\cdot)_k$, indicates it is at timestep k , and for brevity, $(\cdot)_{1:k}$ means a series of vectors (\cdot) 's within the timestep range from 0 to K , which is equivalent to $[(\cdot)_1^T, (\cdot)_2^T, \dots, (\cdot)_K^T]^T$. Other less common symbols will be elucidated the first time they are encountered.

B. Basic Concepts

In this work, we consider a discrete-time, linear and time-varying model as follows:

$$\text{motion model: } \mathbf{x}_k = \mathbf{A}_{k-1} \mathbf{x}_{k-1} + \mathbf{u}_k + \mathbf{w}_k \quad (1)$$

$$\text{observation model: } \mathbf{y}_k = \mathbf{C}_k \mathbf{x}_k + \mathbf{n}_k \quad (2)$$

where k is the discrete-time index with its maximum K . The state vector $\mathbf{x}_k = [\mathbf{p}_k^T, \mathbf{v}_k^T]^T \in \mathbb{R}^6$ consists of 3-dimensional position and velocity, which are the focus of our estimation. The measurements from the sensor system are $\mathbf{y}_k \in \mathbb{R}^m$, where m is the size of it. The transition matrix $\mathbf{A}_{k-1} \in \mathbb{R}^{6 \times 6}$ and the observation matrix $\mathbf{C}_k \in \mathbb{R}^{m \times 6}$ are already known based on historical knowledge. The net input is \mathbf{u}_k , and it is also written as $\mathbf{u}_k = \mathbf{B}_k \mathbf{i}_k$, where $\mathbf{B}_k \in \mathbb{R}^{6 \times s_i}$ is a known control matrix and $\mathbf{i}_k \in \mathbb{R}^{s_i}$ is the original input of size s_i .

The processing and observation noises are formulated as unbiased Gaussian distribution, i.e. $\mathbf{w}_k \sim \mathbf{N}(\mathbf{0}, \mathbf{Q}_k)$ and $\mathbf{n}_k \sim \mathbf{N}(\mathbf{0}, \mathbf{R}_k)$. Also, they are assumed to be uncorrelated. This means $\mathbb{E}[\mathbf{w}_i \mathbf{w}_j^T] = \delta_{ij} \mathbf{Q}_i$, $\mathbb{E}[\mathbf{n}_i \mathbf{n}_j^T] = \delta_{ij} \mathbf{R}_i$ and $[\mathbf{w}_i \mathbf{n}_j^T] = \mathbf{0}$, where $\mathbb{E}[\cdot]$ denotes the mathematical expectation and δ_{ij} is Kronecker- δ function. And $\mathbf{N}(\boldsymbol{\nu}, \mathbf{C})$ represents multivariate Gaussian distribution (a.k.a normal distribution) with probability density function (PDF):

$$\mathbf{N}(\mathbf{x}; \boldsymbol{\nu}, \mathbf{C}) = \frac{\exp\left(-\frac{1}{2}(\mathbf{x} - \boldsymbol{\nu})^T \mathbf{C}^{-1}(\mathbf{x} - \boldsymbol{\nu})\right)}{\sqrt{(2\pi)^k |\mathbf{C}|}} \quad (3)$$

where the \mathbf{x} in front of semicolon is k -dimensional random variable, whereas $\boldsymbol{\nu}$ and \mathbf{C} after semicolon are mean and covariance parameters respectively. The determinant is $|\cdot|$, and the exponent based on natural constant e is denoted by $\exp(\cdot)$. Also in our work, the state \mathbf{x}_k is assumed to be Gaussian, i.e. $\mathbf{x}_k \sim \mathbf{N}(\hat{\mathbf{x}}, \hat{\mathbf{P}})$ or $\mathbf{x}_k \sim \mathbf{N}(\check{\mathbf{x}}, \check{\mathbf{P}})$.

In statistics, the inverse-Wishart distribution is commonly considered as a conjugate prior to the covariance parameter of a multivariate Gaussian distribution with PDF as follows:

$$\mathbf{IW}(\mathbf{C}; \sigma, \boldsymbol{\Sigma}) = \frac{|\boldsymbol{\Sigma}|^{\frac{\sigma}{2}} |\mathbf{C}|^{-\frac{\sigma+n+1}{2}} \exp\left(-\frac{1}{2} \text{tr}(\boldsymbol{\Sigma} \mathbf{C}^{-1})\right)}{2^{\frac{\sigma n}{2}} \Gamma_n\left(\frac{\sigma}{2}\right)} \quad (4)$$

where the random variable \mathbf{C} and the scale matrix $\boldsymbol{\Sigma}$ are $n \times n$ positive-definite matrices. The $\Gamma_n(\cdot)$ means n -dimensional multivariate gamma function, and the σ is the degree of freedom (DoF) parameter.

III. METHODOLOGY

A. Dynamics and Observation Model

Various interference from harsh environments poses a daunting challenge to sensor configuration. The practical application requires both light-weighting and resilience to interference. Under this premise, we deliberately design a sensor system consisting of a single UWB anchor, IMU and optical flow

sensor. The different working conditions for each chosen sensor ensure that a single type of interference, such as dim light or long distance, only affects a specific sensor, leaving the others safe to function effectively. The components are explained as follows.

The IMU collects normalized linear acceleration $\mathbf{a} = [a_x, a_y, a_z]^T$ and normalized quaternion $\mathbf{q} = [q_w, q_x, q_y, q_z]^T$. The rotation matrix is obtained by:

$$\mathbf{R} = 2 \begin{bmatrix} \frac{1}{2} - q_y^2 - q_z^2 & q_x q_y - q_w q_z & q_x q_z + q_w q_y \\ q_x q_y + q_w q_z & \frac{1}{2} - q_x^2 - q_z^2 & q_y q_z - q_w q_x \\ q_x q_z - q_w q_y & q_y q_z + q_w q_x & \frac{1}{2} - q_x^2 - q_y^2 \end{bmatrix} \quad (5)$$

where $\mathbf{R} \in \text{SO}(3)$ is a member of the special orthogonal Lie group. Since the original output acceleration is also normalized, the actual acceleration is obtained by $\mathbf{i} = g\mathbf{R}\mathbf{a} + [0, 0, -g]^T$, where $g \simeq 9.8$ is gravitational acceleration. By pre-integration, the dynamics are formulated as follows:

$$\begin{aligned} \mathbf{x}_k &= \begin{bmatrix} \mathbf{I}_3 & dt \cdot \mathbf{I}_3 \\ \mathbf{0}_3 & \mathbf{I}_3 - dt \cdot \boldsymbol{\mu} \end{bmatrix} \mathbf{x}_{k-1} + \begin{bmatrix} \frac{1}{2} dt^2 \\ dt \end{bmatrix} \otimes \mathbf{i}_k + \mathbb{E}[\mathbf{w}_k] \\ &= \mathbf{A}_{k-1} \mathbf{x}_{k-1} + \mathbf{u}_k \end{aligned} \quad (6)$$

where \otimes is Kronecker product and dt is the time between timestep $k-1$ and k . The $\boldsymbol{\mu} \in \mathbb{R}^{3 \times 3}$ is aerial drag matrix. It will be discussed thoroughly in Subsection III-D, but before that, it is assumed to be already known.

Typically, UWB is a non-linear sensor. For the computational efficiency, it is linearized by:

$$\mathbf{y}_k^{\text{UWB}} = \begin{bmatrix} \tilde{\mathbf{p}}_k^T \\ \|\tilde{\mathbf{p}}_k\|_2 \end{bmatrix} \mathbf{0}_{1 \times 3} \mathbf{x}_k \quad (7)$$

where $\|\cdot\|_2$ is the 2-norm (a.k.a. Euclidean norm). The $\tilde{\mathbf{p}}_k$ is an approximate position calculated via (6):

$$\tilde{\mathbf{p}}_k = [\mathbf{I}_3 \quad \mathbf{0}_3] (\mathbf{A}_{k-1} \tilde{\mathbf{x}}_{k-1} + \mathbf{u}_k) \quad (8)$$

where $\tilde{\mathbf{x}}_{k-1}$ is the output of the last sliding window, and thereby it is known here. The UWB applies a global constraint on our estimator, which suppresses the error accumulation and overcomes the most common interference, vision degradation.

Remark 1: For convenience, we set the origin at the same place as the UWB anchor. Nevertheless, in practical application, since the UWB anchor is fixed w.r.t. world frame, its position can be pre-calibrated easily. If we choose a different origin, by subtracting UWB's position \mathbf{p}_{UWB} from both sides of (8) and adding $\tilde{\mathbf{p}}_k^T \mathbf{p}_{\text{UWB}} / \|\tilde{\mathbf{p}}_k\|_2$ to $\mathbf{y}_k^{\text{UWB}}$, it achieves the same effect as (7).

The optical flow sensor measures velocity, which has no range limitation, and this compensates for the disadvantage of UWB. Typically, the optical flow method only obtains 2-dimensional velocity, which is horizontal velocity. The vertical velocity is obtained by calculating the height difference from a laser unit between each timestep. The observation model is formulated as follows:

$$\mathbf{y}_k = \begin{bmatrix} \mathbf{y}_k^{\text{UWB}} \\ \mathbf{y}_k^{\text{OF}} \end{bmatrix} = \begin{bmatrix} \tilde{\mathbf{p}}_k^T / \|\tilde{\mathbf{p}}_k\|_2 & \mathbf{0}_{1 \times 3} \\ \mathbf{0}_3 & \mathbf{I}_3 \end{bmatrix} \mathbf{x}_k = \mathbf{C}_k \mathbf{x}_k. \quad (9)$$

This system's advantage is that the observation model's position and velocity parts compensate for each other's weaknesses, which guarantees the robustness of measurements and enhances adaptability in changeable environments.

B. Augmented Kalman Filter

This part is the basis of the proposed estimator, which pre-processes all measurements collected by sensors and infor-

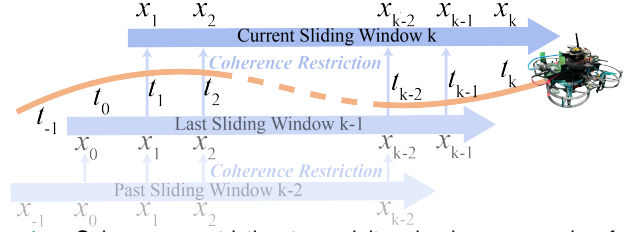


Fig. 1. Coherence restriction to exploit redundancy emerging from overlapping sliding windows.

mation calculated previously by the estimator itself. We exert Kalman filter (KF) during a sliding window. Since every sliding window overlaps each other, we redundantly calculate the posterior state at each timestep many times, as is displayed in Fig. 1. To fully exploit this redundancy, we use an interesting trick to consider our KF as some other kind of sensor. Thus, the measurements, as well as corresponding observation and covariance matrices, are augmented as follows:

$$\tilde{\mathbf{y}}_j = \begin{cases} [\mathbf{y}_j^T, \tilde{\mathbf{x}}_j^T]^T, & j = 1, 2, \dots, k_w - 1 \\ \mathbf{y}_j, & j = k_w \end{cases} \quad (10a)$$

$$\tilde{\mathbf{C}}_j = \begin{cases} [\mathbf{C}_j^T, \mathbf{I}_6]^T, & j = 1, 2, \dots, k_w - 1 \\ \mathbf{C}_j, & j = k_w \end{cases} \quad (10b)$$

$$\tilde{\mathbf{R}}_j = \begin{cases} \text{diag}(\mathbf{R}_j, \tilde{\mathbf{P}}_j), & j = 1, 2, \dots, k_w - 1 \\ \mathbf{R}_j, & j = k_w \end{cases} \quad (10c)$$

where $\text{diag}(\mathbf{A}, \mathbf{B})$ is blockwise diagonal matrix with main diagonal blocks \mathbf{A} and \mathbf{B} .

In this way, we construct our augmented KF as follows:

$$\tilde{\mathbf{P}}_{f,j} = \mathbf{A}_{j-1} \tilde{\mathbf{P}}_{f,j-1} \mathbf{A}_{j-1}^T + \mathbf{Q}_j \quad (11a)$$

$$\tilde{\mathbf{x}}_{f,j} = \mathbf{A}_{j-1} \tilde{\mathbf{x}}_{f,j-1} + \mathbf{u}_j \quad (11b)$$

$$\mathbf{K}_j = \tilde{\mathbf{P}}_{f,j} \tilde{\mathbf{C}}_j^T (\tilde{\mathbf{C}}_j \tilde{\mathbf{P}}_{f,j} \tilde{\mathbf{C}}_j^T + \tilde{\mathbf{R}}_j)^{-1} \quad (11c)$$

$$\hat{\mathbf{P}}_{f,j} = (\mathbf{I} - \mathbf{K}_j \tilde{\mathbf{C}}_j) \tilde{\mathbf{P}}_{f,j} \quad (11d)$$

$$\hat{\mathbf{x}}_{f,j} = \tilde{\mathbf{x}}_{f,j} + \mathbf{K}_j (\tilde{\mathbf{y}}_j - \tilde{\mathbf{C}}_j \tilde{\mathbf{x}}_{f,j}) \quad (11e)$$

where $j = 1, 2, \dots, k_w$. The filter is initialized by $\hat{\mathbf{P}}_{f,0} = \tilde{\mathbf{P}}_0$ and $\hat{\mathbf{x}}_{f,0} = \tilde{\mathbf{x}}_0$. The label f means the \mathbf{x} and \mathbf{P} are only the intermediate temporary variables used to support the forward process, not the estimated posterior state. We will derive posterior states at the beginning of Subsection III-C.

The augmentation in (10) can also be explained as coherence restriction, which forces the estimated state at the same timestep of nearby sliding windows to be as close as possible. Thereby, the numeric stability of the calculation is enhanced. Additionally, all covariance matrices \mathbf{Q} 's and \mathbf{R} 's are set to be the same in each sliding window, which is called consistency restriction. Since $\tilde{\mathbf{R}}_{k_w}$ is different from the other $\tilde{\mathbf{R}}$'s, we denote covariance matrices by different labels $j = 1, 2, \dots, k_w$ to keep the same form as original Kalman.

C. Restricted Inverse-Wishart Smoother

In this subsection, we combine the backward smoother and covariance estimator into a single compact algorithm, restricted inverse-Wishart smoother. We first conduct a backward smoother as follows:

$$\mathbf{G}_j = \hat{\mathbf{P}}_{f,j-1} \mathbf{A}_{j-1}^T \tilde{\mathbf{P}}_{f,j}^{-1} \quad (12a)$$

$$\hat{\mathbf{x}}_{j-1} = \hat{\mathbf{x}}_{f,j-1} + \mathbf{G}_j (\hat{\mathbf{x}}_j - \tilde{\mathbf{x}}_{f,j}) \quad (12b)$$

$$\hat{\mathbf{P}}_{j-1} = \hat{\mathbf{P}}_{f,j-1} + \mathbf{G}_j (\hat{\mathbf{P}}_j - \tilde{\mathbf{P}}_{f,j}) \mathbf{G}_j^T \quad (12c)$$

where $j = k_w, \dots, 2, 1$, with the initial step: $\hat{\mathbf{P}}_{k_w} = \hat{\mathbf{P}}_{f, k_w}$, $\hat{\mathbf{x}}_{k_w} = \hat{\mathbf{x}}_{f, k_w}$. Through this, we obtain our deserved posterior states, which are both the output of the estimator and the basis for the estimation of covariance matrices and aerial drag effect.

As for noise covariance matrices, we first assume they obey inverse-Wishart distribution:

$$p(\hat{\mathbf{Q}}_{k-1} | \hat{\mathbf{x}}_{0:k_w-1}) = \mathbf{IW}(\hat{\mathbf{Q}}_{k-1}; \hat{\phi}_{k-1}, \hat{\mathbf{\Phi}}_{k-1}) \quad (13a)$$

$$p(\hat{\mathbf{R}}_{k-1} | \hat{\mathbf{x}}_{0:k_w-1}) = \mathbf{IW}(\hat{\mathbf{R}}_{k-1}; \hat{\psi}_{k-1}, \hat{\mathbf{\Psi}}_{k-1}) \quad (13b)$$

which are known currently since its label $k-1$ indicates it is the posterior estimation obtained by the last sliding window. The parameters are chosen empirically for the initial step, and hence, the PDFs are also known. In the following equations of this subsection, we use $n = 6$ and $m = 4$ to represent the dimension of state and measurements, respectively, for a consistent form as inverse-Wishart distribution.

According to knowledge of probability theory [31], if the columns of the sample $\mathbf{X} = [\mathbf{x}_1, \mathbf{x}_2, \dots, \mathbf{x}_K]$ are independent and identically distributed n -dimensional Gaussian variables conforming to $\mathbf{N}(\mathbf{0}, \mathbf{C})$, with $\mathbf{C} \sim \mathbf{IW}(\sigma, \mathbf{\Sigma})$, then the conditional PDF is $p(\mathbf{C} | \mathbf{X}) = \mathbf{IW}(\mathbf{C}; \sigma + K, \mathbf{\Sigma} + \mathbf{X}\mathbf{X}^T)$. This is the conjugation nature of inverse-Wishart distribution, and to exploit this, we formulate two auxiliary matrices:

$$\begin{aligned} \tilde{\mathbf{\Phi}}_j = \mathbb{E}[e_{1,j} e_{1,j}^T] &= \hat{\mathbf{P}}_j - \mathbf{A}_{j-1} \mathbf{G}_j \hat{\mathbf{P}}_j - \mathbf{G}_j \hat{\mathbf{P}}_j \mathbf{A}_{j-1}^T \\ &\quad + \mathbf{A}_{j-1} \hat{\mathbf{P}}_{j-1} \mathbf{A}_{j-1}^T + e_{1,j} e_{1,j}^T \end{aligned} \quad (14a)$$

$$\tilde{\mathbf{\Psi}}_j = \mathbb{E}[e_{2,j} e_{2,j}^T] = \mathbf{C}_j \hat{\mathbf{P}}_j \mathbf{C}_j^T + e_{2,j} e_{2,j}^T \quad (14b)$$

where the error terms are $e_{1,j} = \hat{\mathbf{x}}_j - \mathbf{A}_{j-1} \hat{\mathbf{x}}_{j-1} - \mathbf{u}_j$ and $e_{2,j} = \mathbf{y}_j - \mathbf{C}_j \hat{\mathbf{x}}_j$. By applying the conjugation nature, we obtain the posterior noise covariance matrices as follows:

$$\hat{\phi}_k = w_1(\hat{\phi}_{k-1} - n - 1) + n + 1 + w_2 k_w \quad (15a)$$

$$\hat{\psi}_k = w_1(\hat{\psi}_{k-1} - m - 1) + m + 1 + w_2 k_w \quad (15b)$$

$$\hat{\mathbf{\Phi}}_k = w_1 \hat{\mathbf{\Phi}}_{k-1} + w_2 \sum_{j=1}^{k_w} \tilde{\mathbf{\Phi}}_j \quad (15c)$$

$$\hat{\mathbf{\Psi}}_k = w_1 \hat{\mathbf{\Psi}}_{k-1} + w_2 \sum_{j=1}^{k_w} \tilde{\mathbf{\Psi}}_j \quad (15d)$$

where $w_1, w_2 \in [0, 1]$ are weights to balance the features extracted during the previous and current sliding windows.

To further suppress potential divergence led by malfunctioning sensors, we apply an additional weight to the updating process of observation noise covariance. The sum of its auxiliary matrices is calculated in iterative form:

$$\sum_{j=1}^{k_j} \tilde{\mathbf{\Psi}}_j = w_3 \left(\sum_{j=1}^{k_j-1} \tilde{\mathbf{\Psi}}_j + \tilde{\mathbf{\Psi}}_{k_j} \right) \quad (16)$$

where $k_j = 1, 2, \dots, k_w$ and $w_3 \in (0, 1)$.

To find proper weights, we need to evaluate the error during the calculation process. Assuming the initial state is biased as $\hat{\mathbf{x}}_{f,0} = \bar{\mathbf{x}}_0 + \delta \mathbf{x}_0$, and the final state is $\hat{\mathbf{x}}_{f,k_w} = \bar{\mathbf{x}}_{k_w} + \delta \mathbf{x}_{k_w}$. By iteratively conducting the augmented Kalman filter, the error propagation relation is obtained:

$$\delta \mathbf{x}_{k_w} = \left(\prod_{j=1}^{k_w} (\mathbf{I} - \mathbf{K}_j \tilde{\mathbf{C}}_j) \mathbf{A}_{j-1} \right) \delta \mathbf{x}_0 = \mathbf{E} \delta \mathbf{x}_0. \quad (17)$$

Hence, we exploit the error propagation matrix \mathbf{E} in two ways:

$$\text{average trace: } \bar{\lambda} = \text{tr}(\mathbf{E})/6 \quad (18a)$$

$$\text{reduced determinant: } \varrho = \sqrt[6]{|\mathbf{E}|} \quad (18b)$$

where $\text{tr}(\cdot)$ is the trace of square matrix (\cdot) .

For w_1 and w_2 , if $\bar{\lambda}$ is larger than a threshold $\lambda_0 \in (0, 1]$, this means the estimation is too bad to be used in covariance adjustment. And we set $w_1 = 1$ and $w_2 = 0$, so that $\hat{\mathbf{Q}}_k$ and $\hat{\mathbf{R}}_k$ remain unchanged. However, if $\bar{\lambda} < \lambda_0$, we can adjust covariance matrices, and the weights are calculated as $w_1 = 1 - f_1 \bar{\lambda}$ and $w_2 = 1 - f_1 + f_1 \bar{\lambda}$, where $f_1 \in (0, 1)$ is a factor to control how fast the weights change. As for w_3 , we set $w_3 = f_2 + \varrho/f_2$, where $f_2 \in (0, 1)$ is another factor to control change speed. This is the error propagation restriction, whose necessity and effectiveness will be thoroughly discussed in Subsection IV-C. In this way, the deserved posterior PDFs are obtained. The posterior noise covariance matrices are calculated as mathematical expectations:

$$\mathbf{Q}_k = \mathbb{E}[\hat{\mathbf{Q}}_k] = (\hat{\phi}_k - n - 1)^{-1} \hat{\mathbf{\Phi}}_k \quad (19a)$$

$$\bar{\mathbf{R}}_k = \mathbb{E}[\hat{\mathbf{R}}_k] = (\hat{\psi}_k - m - 1)^{-1} \hat{\mathbf{\Psi}}_k. \quad (19b)$$

In practice, the message from the sensor may be lost, or the data quality may be poor sometimes, whereas the adaptive adjustment cannot catch up with the fast change. To handle this, a boolean amendment is included to represent the work condition of sensors:

$$\mathbf{S}_{k,i} = \begin{cases} \mathbf{I}_s, & \text{the } i\text{-th sensor functions normally} \\ \varepsilon \mathbf{I}_s, & \text{the } i\text{-th sensor malfunctions} \end{cases} \quad (20)$$

where s is the dimension of the output from the i -th sensor, and ε is a very large number. We have $\mathbf{S}_{k,1} \in \mathbb{R}$ and $\mathbf{S}_{k,2} \in \mathbb{R}^{3 \times 3}$ represents the work condition of the UWB and optical flow sensor respectively. The noise covariance matrices for practical application are finally obtained by combining (19b) and (20) together: $\mathbf{R}_k = \mathbf{S}_k \bar{\mathbf{R}}_k \mathbf{S}_k$, where $\mathbf{S}_k = \text{diag}(\mathbf{S}_{k,1}, \mathbf{S}_{k,2})$. The algorithm of inverse-Wishart smoother in each sliding window is illustrated in Algorithm 1.

D. Aerial Drag Estimator

As is discussed in the introduction, the aerial drag effect is essential, but its estimation is high-cost due to the complexity of the UAV's aerodynamics. Thanks to the proposed sensor system, we have enough data to indirectly evaluate the aerial drag effect. We develop a novel aerial drag estimator, which omits intricate aerodynamics and spares computational resources. First, consider the velocity part of the prior state obtained by dynamics (6): $\check{\mathbf{v}}_j = (\mathbf{I}_3 - dt \cdot \boldsymbol{\mu}) \hat{\mathbf{v}}_{j-1} + dt \cdot \mathbf{i}_k$, where $\check{\mathbf{v}}_j$ and $\hat{\mathbf{v}}_{j-1}$ are velocity part of $\check{\mathbf{x}}_j$ and $\hat{\mathbf{x}}_{j-1}$ respectively. Also, with measurements from the sensor system, we obtain posterior $\hat{\mathbf{v}}_j$. Our goal is to adjust $\boldsymbol{\mu}$ such that $\check{\mathbf{v}}_j$ approaches $\hat{\mathbf{v}}_j$, and hence we can formulate a cost function in quadratic form w.r.t. $\boldsymbol{\mu}$: $J_j = \|\hat{\mathbf{v}}_j - \check{\mathbf{v}}_j\|_2^2 = (\hat{\mathbf{v}}_j - \check{\mathbf{v}}_j)^T (\hat{\mathbf{v}}_j - \check{\mathbf{v}}_j)$. By taking the derivative:

$$\left. \frac{\partial J_j}{\partial \boldsymbol{\mu}} \right|_{\hat{\mathbf{v}}_{j-1}, \hat{\mathbf{v}}_j} = 2dt (\hat{\mathbf{v}}_j - (\mathbf{I}_3 - dt \boldsymbol{\mu}) \hat{\mathbf{v}}_{j-1} - dt \mathbf{i}_j) \hat{\mathbf{v}}_{j-1}^T, \quad (21)$$

we can conduct a gradient descent method to amend $\boldsymbol{\mu}$:

$$\boldsymbol{\mu} \leftarrow \boldsymbol{\mu} - \ell_k \cdot \left. \frac{\partial J_j}{\partial \boldsymbol{\mu}} \right|_{\hat{\mathbf{v}}_{j-1}, \hat{\mathbf{v}}_j} \quad (22)$$

where ℓ_k is step length.

Since choosing the proper step length is a critical problem in

Algorithm 1: Restricted Inverse-Wishart Smoother at Timestep k of $\mathcal{O}(k_w(n^3 + n^2m + m^2))$

Input: $\tilde{\mathbf{x}}_{k-k_w:k-1}$, $\tilde{\mathbf{P}}_{k-k_w:k-1}$, $\mathbf{A}_{k-k_w:k-1}$,
 $\mathbf{u}_{k-k_w+1:k}$, $\mathbf{y}_{k-k_w+1:k}$, $\mathbf{C}_{k-k_w+1:k}$, $\hat{\phi}_{k-1}$,
 $\hat{\Phi}_{k-1}$, $\hat{\psi}_{k-1}$, $\hat{\Psi}_{k-1}$, \mathbf{E} , \mathbf{S}_k
Parameter: k_w , λ_0 , f_1 , f_2 , ε , $n = 6$, $m = 4$
Output: $\hat{\mathbf{x}}_{0:k_w}$, $\hat{\mathbf{P}}_{0:k_w}$, $\hat{\phi}_k$, $\hat{\Phi}_k$, $\hat{\psi}_k$, $\hat{\Psi}_k$, \mathbf{Q}_k , \mathbf{R}_k

- 1 $\bar{\lambda} \leftarrow \frac{1}{6}\text{tr}(\mathbf{E})$ and $\varrho \leftarrow \sqrt[6]{|\mathbf{E}|}$;
- 2 **if** $\bar{\lambda} \geq \lambda_0$ **then**
- 3 $w_1 \leftarrow 1$ and $w_2 \leftarrow 0$;
- 4 **else**
- 5 $w_1 \leftarrow 1 - f_1\bar{\lambda}$ and $w_2 \leftarrow 1 - f_1 + f_1\bar{\lambda}$;
- 6 **end**
- 7 $w_3 \leftarrow f_2 + \varrho/f_2$;
- 8 $\hat{\mathbf{P}}_{k_w} \leftarrow \hat{\mathbf{P}}_{f,k_w}$ and $\hat{\mathbf{x}}_{k_w} \leftarrow \hat{\mathbf{x}}_{f,k_w}$;
- 9 **for** $j = k - 1 : k - k_w + 1$ **do**
- 10 Conduct backward smoother iteration by (12);
- 11 Calculate auxiliary matrices by (14) and (16);
- 12 **end**
- 13 Calculate shape and DoF parameters by (15);
- 14 Calculate \mathbf{Q} and $\bar{\mathbf{R}}$ by (19);
- 15 $\mathbf{R}_k \leftarrow \mathbf{S}_k \bar{\mathbf{R}}_k \mathbf{S}_k$;

gradient descent, we design a strategy to accomplish this. The noise covariance matrices inherently reflect the deviation of dynamics and observation model w.r.t. actual situation. Hence, they are natural indicators to evaluate the performance of both models. Under this premise, we calculate ℓ_k as follows:

$$\ell_k = \begin{cases} 0, & \sqrt[6]{|\mathbf{Q}_k|} \leq \sqrt[4]{|\mathbf{R}_k|} \\ b_u - \frac{(b_u - b_l)\sqrt[4]{|\mathbf{R}_k|}}{\sqrt[6]{|\mathbf{Q}_k|}}, & \sqrt[6]{|\mathbf{Q}_k|} > \sqrt[4]{|\mathbf{R}_k|} \end{cases} \quad (23)$$

where b_u and b_l are upper and lower bounds for step length. Intuitively, if $\sqrt[6]{|\mathbf{Q}_k|} \leq \sqrt[4]{|\mathbf{R}_k|}$, the sensors are less reliable than the dynamics, and hence we should not amend $\boldsymbol{\mu}$ with measurements. On the other hand, once $\sqrt[6]{|\mathbf{Q}_k|} > \sqrt[4]{|\mathbf{R}_k|}$, we can start our adjustment. And as $\sqrt[4]{|\mathbf{R}_k|}$ gets smaller, ℓ grows from its lower bound to upper bound.

Finally, we compress all three parts—augmented Kalman filter, restricted inverse-Wishart smoother and aerial drag estimator, into a single compact algorithm, restricted adaptive sliding window estimator (RASWE). The Algorithm 2 is the pseudo-code version of the proposed method RASWE.

IV. EXPERIMENTS

A. Experimental Setup

In all experiments, a VICON[®] motion capture system is employed to record ground truth with a frequency of 200Hz. The quadrotor unmanned aerial vehicle is steered under the control of the open-source Pixhawk[®]. The onboard computer is an NVIDIA[®] NX computing mounted Intel Atom x7 (four cores, 1.8 GHz). The IMU (module CHCNAV CL-510) is utilized for acceleration measurements. The Nooploop[®] UWB (module LinkTrack LTPS[®]) is selected for range measurement cooperated with a fixed anchor also equipped with the same UWB. The optical flow sensor (module NiMing v4) is adopted for velocity measurements. The IMU, UWB, and optical flow measurements are collected at 25Hz. Since this section is

Algorithm 2: Restricted Adaptive Sliding Window Estimator at Timestep k of $\mathcal{O}(k_w(n^3 + n^2m + nm^2 + m^3))$

Input: $\tilde{\mathbf{x}}_{k-k_w:k-1}$, $\tilde{\mathbf{P}}_{k-k_w:k-1}$, $\boldsymbol{\mu}$, dt , $\mathbf{u}_{k-k_w+1:k}$,
 $\mathbf{y}_{k-k_w+1:k}$, $\hat{\phi}_{k-1}$, $\hat{\Phi}_{k-1}$, $\hat{\psi}_{k-1}$, $\hat{\Psi}_{k-1}$, \mathbf{S}_k
Parameter: k_w , λ_0 , f_1 , f_2 , ε , b_l , b_u , $n = 6$, $m = 4$
Output: $\hat{\mathbf{x}}_{k-k_w:k}$, $\hat{\phi}_k$, $\hat{\Phi}_k$, $\hat{\psi}_k$, $\hat{\Psi}_k$, $\boldsymbol{\mu}$

- 1 Calculate \mathbf{Q}_k and $\bar{\mathbf{R}}_k$ by (19);
- 2 $\mathbf{R}_k \leftarrow \mathbf{S}_k \bar{\mathbf{R}}_k \mathbf{S}_k$;
- 3 Calculate $\mathbf{A}_{k-k_w:k-1}$ by (6);
- 4 Calculate $\mathbf{C}_{k-k_w+1:k}$ by (8) and (9);
- 5 Augment $\mathbf{y}_{k-k_w+1:k}$, $\mathbf{C}_{k-k_w+1:k}$ and \mathbf{R}_k by (10);
- 6 $\hat{\mathbf{P}}_{f,0} \leftarrow \tilde{\mathbf{P}}_0$ and $\hat{\mathbf{x}}_{f,0} \leftarrow \tilde{\mathbf{x}}_0$;
- 7 **for** $j = k - k_w + 1 : +1 : k$ **do**
- 8 Conduct Kalman filter by (11);
- 9 **end**
- 10 Calculate \mathbf{E} by (17);
- 11 Run Algorithm 1;
- 12 Calculate step length by (23);
- 13 **for** $j = k - k_w + 1 : +1 : k$ **do**
- 14 Calculate derivative by (21);
- 15 Update $\boldsymbol{\mu}$ by (22);
- 16 **end**

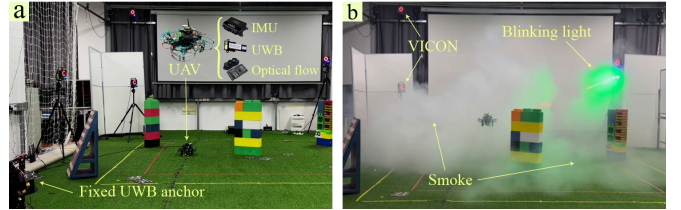


Fig. 2. Testbeds of experiments. Subfigure (a) shows common surroundings; subfigure (b) is a smoky and blinking environment.

mainly focused on the performance of state estimation, the design of the controller is simplified.

We conduct experiments with different velocities in common laboratory surroundings and record three datasets \mathbf{B}_1 to \mathbf{B}_3 . To evaluate our method in harsh environments, we repeat experiments with blinking light and a smoke generator, and record four datasets \mathbf{Y}_0 to \mathbf{Y}_3 . To overcome jagged edges in data due to the simplified controller and poor physical structure lacking vibration damping, we apply a Savitzky–Golay filter with polynomial order 3 and frame length 9 to the estimated position. The configuration of the testbed is illustrated in Fig. 2. The parameters in experiments are displayed in Table I.

B. Evaluation of Overall Performance

To assess the effectiveness and stability of the proposed method, we compare it to the DWE in [32], which is equivalent

TABLE I
PARAMETERS AND INITIAL VALUES OF ESTIMATOR IN EXPERIMENTS

| Item | Value | Item | Initial Value |
|---------------|--------------------|------------------------|--------------------------|
| k_w | 10 | $\boldsymbol{\mu}_0$ | diag(0.2, 0.2, 0.8) |
| λ_0 | 1×10^{-3} | $\tilde{\mathbf{P}}_0$ | $0.1 \cdot \mathbf{I}_6$ |
| f_1 | 1×10^{-2} | $\tilde{\mathbf{x}}_0$ | VICON ground truth |
| f_2 | 0.1 | $\hat{\Phi}_0$ | $17 \cdot \mathbf{I}_6$ |
| b_u | 1×10^{-2} | $\hat{\phi}_0$ | 10 |
| b_l | 1×10^{-3} | $\hat{\Psi}_0$ | $13 \cdot \mathbf{I}_4$ |
| ε | 1×10^3 | $\hat{\psi}_0$ | 8 |

TABLE II

OVERALL PERFORMANCE COMPARISON BETWEEN DWE AND RASWE

| Data Set | Method | RMSE (meter) | | | STD (meter) | | |
|----------------|--------|--------------|------|------|-------------|------|------|
| | | x | y | z | x | y | z |
| B ₁ | DWE | 0.07 | 0.14 | 0.05 | 0.04 | 0.07 | 0.03 |
| | RASWE | 0.07 | 0.14 | 0.03 | 0.04 | 0.09 | 0.02 |
| B ₂ | DWE | 0.08 | 0.13 | 0.06 | 0.05 | 0.08 | 0.02 |
| | RASWE | 0.09 | 0.11 | 0.05 | 0.06 | 0.07 | 0.02 |
| B ₃ | DWE | 0.24 | 0.38 | 0.11 | 0.15 | 0.19 | 0.06 |
| | RASWE | 0.14 | 0.11 | 0.05 | 0.10 | 0.07 | 0.03 |
| Y ₀ | DWE | 0.32 | 0.62 | 0.09 | 0.20 | 0.38 | 0.05 |
| | RASWE | 0.25 | 0.25 | 0.05 | 0.15 | 0.17 | 0.03 |
| Y ₁ | DWE | 0.19 | 0.43 | 0.06 | 0.11 | 0.26 | 0.03 |
| | RASWE | 0.23 | 0.22 | 0.08 | 0.13 | 0.14 | 0.06 |
| Y ₂ | DWE | 0.17 | 0.35 | 0.10 | 0.10 | 0.26 | 0.08 |
| | RASWE | 0.22 | 0.19 | 0.15 | 0.11 | 0.13 | 0.12 |
| Y ₃ | DWE | 0.39 | 0.43 | 0.24 | 0.23 | 0.27 | 0.22 |
| | RASWE | 0.37 | 0.38 | 0.06 | 0.25 | 0.25 | 0.04 |

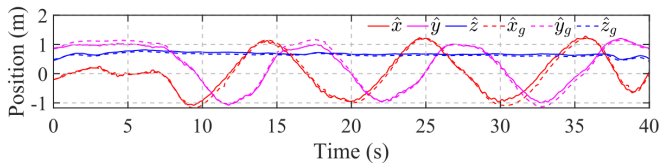


Fig. 3. Typical position estimation results of RASWE on dataset B₂, where dotted line and label "g" are used to denote ground truth from VICON.

to the combination of augmented Kalman filter (11) and backward smoother (12) without adjusting parameters like covariance and aerial drag matrices. The results are displayed in Table II, where we evaluate the root mean square error (RMSE) and the standard deviation (STD) along three axes.

From the results, it proves the proposed method RASWE outperforms DWE, especially in harsh environments, Y₀ to Y₃. In common environments, however, RASWE may not always show its advantage since the noise covariance matrices and aerial drag matrix seldom change much. The typical estimation results of dataset B₂ is illustrated in Fig. 3. Notably, RASWE reduces the error along the x-axis and y-axis to the same degree, whereas DWE always leaves one axis worse. This is because noise covariance matrices are natural weights, and RASWE adjusts them accordingly to balance the error. But without adaptive adjustment, the weights of two axes are empirically set to be the same, which conflicts with the fact and causes performance degradation of DWE.

As illustrated in subfigure (a) of Fig. 4, for the typical experiment B₂, the diagonal entry of the process noise covariance matrix corresponding to the y-axis is more significant than that corresponding to the x-axis, which is consistent with DWE result that RMSE along the y-axis is more significant than that along the x-axis. Although the symmetry of aerodynamics indicates the weights corresponding to the x-axis and y-axis should be the same, the measurements from UWB cause this difference. It only provides distance information, a weak constraint of only one dimension. The limited dimension of information leads to the fact that, in practice, estimation along one axis usually performs worse. On the other hand, it is an optical flow sensor that plays a part in velocity estimation, while UWB does not affect this process. Hence, we see $Q_{44} = Q_{55}$, which agrees with the symmetry of aerodynamics.

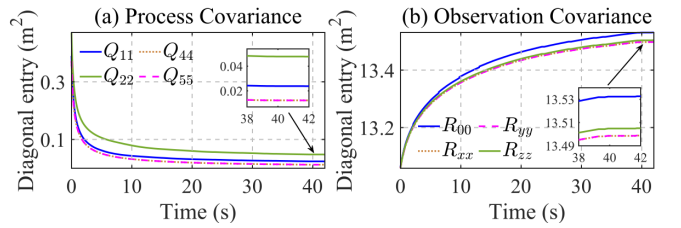


Fig. 4. Diagonal entry changing tendency of noise covariance matrices (dataset: B₂). Subfigure (a) shows entries of process noise covariance matrices where Q_{11} , Q_{22} , Q_{44} and Q_{55} correspond to x-position, y-position, x-velocity and y-velocity respectively; subfigure (b) shows entries of the shape parameter of observation noise covariance where R_{00} corresponds to UWB while the others correspond to three axes of the optical flow sensor.

TABLE III

RMSE COMPARISON BETWEEN MODIFIED RASWEs WITH CERTAIN RESTRICTION CANCELLED (UNIT: METER)

| Cancelled Restriction | B ₁ | B ₂ | B ₃ | Y ₀ | Y ₁ | Y ₂ | Y ₃ |
|-----------------------|----------------|----------------|----------------|----------------|----------------|----------------|----------------|
| None | 0.16 | 0.15 | 0.19 | 0.35 | 0.33 | 0.33 | 0.54 |
| ErrProp | 0.16 | 0.15 | 0.20 | 0.45 | 0.45 | 0.43 | 0.59 |
| coherence | 1.27 | 1.04 | 1.49 | 1.50 | 1.44 | 1.55 | 1.78 |
| Consist | 0.94 | 1.04 | 4.04 | 1.57 | 2.28 | 1.23 | 1.83 |

Thanks to our algorithm, the process noise covariance matrix becomes competent in revealing these points, which helps the estimator find more proper weights.

For observation noise covariance matrix in subfigure (b), we evaluate its shape parameter here instead of the covariance matrix itself since its change is slight and uneasy for intuitive understanding ought to error propagation restriction (16). It shows that the entry corresponding to UWB is the largest one because this range of odometry is not always sufficiently accurate and can only provide a global reference. As for the optical flow sensor, entries of the x-axis and y-axis are the same due to symmetry, and the entry of the z-axis is slightly larger than theirs since vertical velocity obtained by the difference method is less precise than horizontal velocity obtained by the optical flow method. In this way, RASWE makes full use of information from sensors and tries its best to avoid divergence led by malfunctioning sensors.

C. Validation of Inherent Restrictions

As mentioned before, we apply several inherent restrictions to overcome sensor malfunction and suppress potential divergence. In this subsection, we delve into the effects of them. Here we evaluate three axes together using RMSE of Euclidean distance between estimated position and ground truth, $\sqrt{\frac{1}{n} \sum_{i=1}^n \|\mathbf{p}_i - \mathbf{p}_{i,g}\|_2^2}$, instead of examining three separated axes. All results are displayed in Table III, where "none" denotes original RASWE the same as that in Table II.

Among all restrictions, the most complicated one is error propagation restriction (abbr. ErrProp or EP), (17) and (18). We cancel this restriction by setting three weights in (15) and (16) to be 1, $w_1 = w_2 = w_3 = 1$. From the results, we see that in common environments, whether to cancel it or not does not affect estimation precision much. In harsh environments, however, the estimation deteriorates after the restriction is canceled. This shows RASWE's advantage in handling harsh environments, as shown in Fig. 5. Without error propagation restriction, the estimator can hardly track the

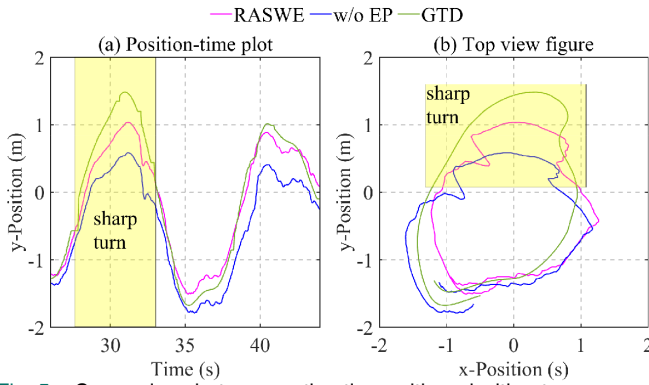


Fig. 5. Comparison between estimations with and without error propagation restriction on the sharp turn of dataset Y_2 , where "GTD" means ground truth data.

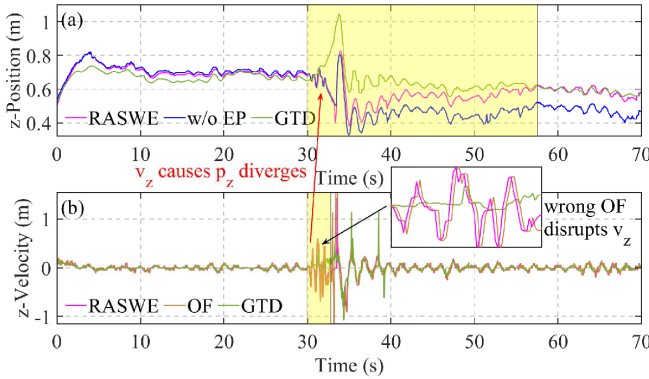


Fig. 6. Position and velocity estimation of RASWE on dataset Y_1 with sudden rapid fluctuations, where "GTD" means ground truth data. Subfigure (a) is a comparison along the z-axis; subfigure (b) shows the reason for the divergence and recovery of position estimation.

position, especially when the UAV takes a sharp turn because it has been used for mild movement.

Another perspective is illustrated in Fig. 6. The estimation is initially interfered with by sudden rapid fluctuations, and RASWE gradually recovers from divergence. In contrast, the one without restriction is misled by malfunctioning sensors, leaving an estimation bias. The root cause of position estimation divergence is the divergence of velocity estimation shown in subfigure (b). The height laser of the optical flow sensor (abbr. OF) mistakes smoke particles as ground and measures the wrong z-velocity, which misleads velocity estimation. Thanks to error propagation restriction, velocity estimation converges again soon, which results in gradual convergence of position estimation through integral relation.

Aerial drag adjustment is also affected at the beginning of sudden fluctuations since the calculation of its gradient (21) relies directly on velocity estimation. The changing tendency of aerial drag adjustment on dataset Y_1 is illustrated in subfigure (a) of Fig. 7. A sharp increasing curve emerges at first due to fluctuations, but soon later, it is replaced by a horizontal line. This is because those wrong adaptive adjustments are stopped by error propagation restriction, and subfigure (b) shows how parameters respond to fluctuations. Soon after rapid fluctuations, adjustments continue and converge again. Notably, the details of the convergent line show slight oscillation at the micro-scale even if it seems horizontal in subfigure (a), which is different from the horizontal line resulting from error propagation restriction.

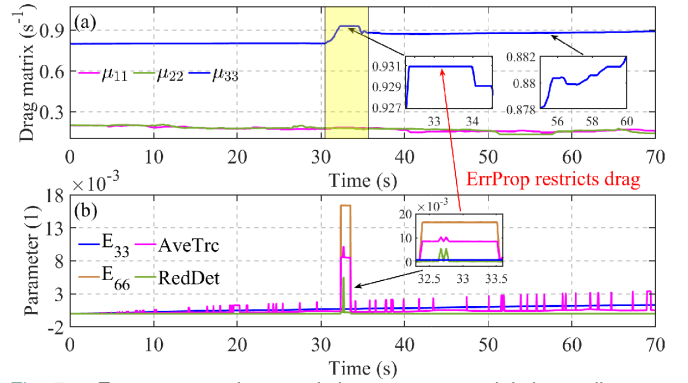


Fig. 7. Error propagation restriction prevents aerial drag adjustment from divergence (dataset Y_1). Subfigure (a) illustrates the changing tendency of aerial drag coefficients. Subfigure (b) displays the changing tendency of parameters in (18) and diagonal entry of the error propagation matrix in (17).

The error propagation matrix acutely perceives anomalous estimation. As is shown in subfigure (b) of Fig. 7, the diagonal entry corresponding to z-velocity, E_{66} , responds to sudden fluctuations. However, the entry corresponding to the z-position, E_{33} , remains almost unchanged. That is because position estimation is based on velocity estimation via integral, and the calculation process is normal, although the results are misleading. This shows the proficiency of E in (17) to serve as an online error inspector. The parameters in (18) are also displayed in subfigure (b), where the average trace (abbr. AveTrc) is more sensitive to slight interference, and the reduced determinant (abbr. RedDet) focuses on significant fluctuations more. This proves effective in merging these two parameters in error propagation restriction. The second restriction is coherence restriction, which exploits redundant information due to overlapping sliding windows, as illustrated in Fig. 1. We remove it by simply omitting the augmentation step for KF (10). Our estimator relies on coherence restriction to inherit historical information since the sliding window size is 10 in our experiments, which is typically too small to perform proper estimation. Hence, as is shown in Table II, every estimation has a significant error if the coherence restriction is canceled.

To keep numerical stability, we apply one additional restriction called consistency restriction. When RASWE begins in every new sliding window, we re-initialize $\hat{P}_0 = 0.1 \cdot I_6$. We keep all Q 's and \tilde{R} 's the same for every timestep, which is obtained by Algorithm 1 in the last sliding window. To cancel this restriction, we use a matrix sequence of size $k_w + 1$ to record historical covariance matrices P 's, Q 's and R 's. In this way, all the noise covariance matrices at each timestep differ. Hence, the estimator becomes more numerically sensitive, increasing the divergence probability. This counts for the results that diverge badly. On the other hand, since the sliding window size is quite small, it is rational to assume all covariance matrices are approximately the same.

The conclusion is that coherence and consistency restrictions are indispensable for our estimator. Error propagation restriction is essential to handle harsh environments, significantly suppressing divergence.

V. CONCLUSION

In this paper, we propose a restricted adaptive sliding window estimator using a single anchor for UAV positioning in harsh environments, which simultaneously estimates the states, noise covariance matrices and aerial drag. Our work differs from existing adaptive estimators in two ways. First, we introduce an error propagation matrix to assess estimation performance online, and we accordingly impose inherent restrictions to mitigate potential divergence caused by sensor malfunctions. Secondly, we develop an adaptive aerial drag estimator to adjust the motion model dynamically, enhancing overall performance. Experiments validate the effectiveness of the estimator. Our proposed method achieves an average RMSE of 0.17m in common environments and 0.39m in harsh environments, outperforming the state-of-the-art in blinking and smoky environments. The covariance estimation strongly tracks the statistic features of dynamics and observation model noises, which overcomes the asymmetry of single anchor estimation. The error propagation restriction demonstrates its proficiency in suppressing divergence when handling abrupt changes like sharp turns and sudden trajectory fluctuations.

In the future, we will enhance the adaptability of the estimator, considering lumped vibrations from the flight controller.

REFERENCES

- [1] R. La Scalea, M. Rodrigues, D. P. M. Osorio, C. H. Lima, R. D. Souza, H. Alves, and K. C. Branco, "Opportunities for autonomous uav in harsh environments," in *2019 16th International Symposium on Wireless Communication Systems (ISWCS)*, 2019, pp. 227–232.
- [2] B. Peng, Y. Chen, T. Zheng, C. Duan, and Z. Yao, "Safety positioning for uav swarms in harsh environments," *IEEE Network*, vol. 36, no. 4, pp. 46–53, 2022.
- [3] L. Zhang, J. Chen, C. Wu, Q. Qie, and Y. Jin, "Uav path planning based on vision," in *2023 IEEE International Conference on Unmanned Systems (ICUS)*, 2023, pp. 7–10.
- [4] M. Rezinikina, O. Rezinikina, and A. Zaporozhets, "Uavs application in power engineering," in *2021 IEEE 6th International Conference on Actual Problems of Unmanned Aerial Vehicles Development (APUAVD)*, 2021, pp. 161–164.
- [5] Y. Gao and G. Li, "A gnss instrumentation covert directional spoofing algorithm for uav equipped with tightly-coupled gnss/imu," *IEEE Transactions on Instrumentation and Measurement*, vol. 72, pp. 1–13, 2023.
- [6] X. Zhou, Y. Chen, Y. Liu, and J. Hu, "A novel sensor fusion method based on invariant extended kalman filter for unmanned aerial vehicle," in *2021 IEEE International Conference on Robotics and Biomimetics (ROBIO)*, 2021, pp. 1111–1116.
- [7] J.-T. Zou, C.-Y. Wang, and Y. M. Wang, "The development of indoor positioning aerial robot based on motion capture system," in *2016 International Conference on Advanced Materials for Science and Engineering (ICAMSE)*, 2016, pp. 380–383.
- [8] T. Pavlenko, M. Schütz, M. Vossiek, T. Walter, and S. Montenegro, "Wireless local positioning system for controlled uav landing in gnss-denied environment," in *2019 IEEE 5th International Workshop on Metrology for AeroSpace (MetroAeroSpace)*, 2019, pp. 171–175.
- [9] Z. Wang, S. Liu, G. Chen, and W. Dong, "Robust visual positioning of the uav for the under bridge inspection with a ground guided vehicle," *IEEE Transactions on Instrumentation and Measurement*, vol. 71, pp. 1–10, 2022.
- [10] A. Marut, P. Wojciechowski, K. Wojtowicz, and K. Falkowski, "Visual-based landing system of a multirotor uav in gnss denied environment," in *2023 IEEE 10th International Workshop on Metrology for AeroSpace (MetroAeroSpace)*, 2023, pp. 308–313.
- [11] Z. Jiang, J. Tan, D. Huang, and Y. Meng, "Robust visual positioning of the uav for the regional operation," in *2023 CAA Symposium on Fault Detection, Supervision and Safety for Technical Processes (SAFEPROCESS)*, 2023, pp. 1–5.
- [12] L. Yu, E. Yang, B. Yang, Z. Fei, and C. Niu, "A robust learned feature-based visual odometry system for uav pose estimation in challenging indoor environments," *IEEE Transactions on Instrumentation and Measurement*, vol. 72, pp. 1–11, 2023.
- [13] S. W. Chen, G. V. Nardari, E. S. Lee, C. Qu, X. Liu, R. A. F. Romero, and V. Kumar, "Sloam: Semantic lidar odometry and mapping for forest inventory," *IEEE Robotics and Automation Letters*, vol. 5, no. 2, pp. 612–619, 2020.
- [14] B. Yang, E. Yang, L. Yu, and A. Loeliger, "High-precision uwb-based localisation for uav in extremely confined environments," *IEEE Sensors Journal*, vol. 22, no. 1, pp. 1020–1029, 2022.
- [15] Q. Zeng, Y. Jin, H. Yu, and X. You, "A uav localization system based on double uwb tags and imu for landing platform," *IEEE Sensors Journal*, vol. 23, no. 9, pp. 10 100–10 108, 2023.
- [16] K. Li, S. Bu, Y. Dong, Y. Wang, X. Jia, and Z. Xia, "Uwb-vo: Ultra-wideband anchor assisted visual odometry," in *2023 IEEE International Conference on Unmanned Systems (ICUS)*, 2023, pp. 943–950.
- [17] Q. Zeng, H. Yu, X. Ji, X. Tao, and Y. Hu, "Fast and robust semidirect monocular visual-inertial odometry for uav," *IEEE Sensors Journal*, vol. 23, no. 20, pp. 25 254–25 262, 2023.
- [18] P.-Y. Kao, H.-J. Chang, K.-W. Tseng, T. Chen, H.-L. Luo, and Y.-P. Hung, "Viunet: Deep visual-inertial-uwb fusion for indoor uav localization," *IEEE Access*, vol. 11, pp. 61 525–61 534, 2023.
- [19] T. H. Nguyen, T.-M. Nguyen, and L. Xie, "Range-focused fusion of camera-imu-uwb for accurate and drift-reduced localization," *IEEE Robotics and Automation Letters*, vol. 6, no. 2, pp. 1678–1685, 2021.
- [20] C. Jiang, S. Zhang, H. Li, and Z. Li, "Performance evaluation of the filters with adaptive factor and fading factor for gnss/ins integrated systems," *GPS Solutions*, vol. 25, no. 4, p. 130, Jul 2021. [Online]. Available: <https://doi.org/10.1007/s10291-021-01165-4>
- [21] Q. Pan, Y. Zhang, and Y. Liu, "Fuzzy adaptive extended kalman filter slam algorithm based on the improved pso algorithm," in *2019 Chinese Automation Congress (CAC)*, 2019, pp. 3488–3493.
- [22] A. Dey, "Adaptive cubature kalman filter for bearing only tracking with non-additive sensor noise," in *2020 International Conference on Emerging Trends in Information Technology and Engineering (ic-ETITE)*, 2020, pp. 1–6.
- [23] C. Jiang, Z. Wang, H. Liang, and Y. Wang, "A novel adaptive noise covariance matrix estimation and filtering method: Application to multi-object tracking," *IEEE Transactions on Intelligent Vehicles*, vol. 9, no. 1, pp. 626–641, 2024.
- [24] F. Zhu, Y. Huang, C. Xue, L. Mihaylova, and J. Chambers, "A sliding window variational outlier-robust kalman filter based on student's t-noise modeling," *IEEE Transactions on Aerospace and Electronic Systems*, vol. 58, no. 5, pp. 4835–4849, 2022.
- [25] S. Qiao, Y. Fan, G. Wang, D. Mu, and Z. He, "Modified strong tracking slide window variational adaptive kalman filter with unknown noise statistics," *IEEE Transactions on Industrial Informatics*, vol. 19, no. 8, pp. 8679–8690, 2023.
- [26] M. Vaishnavi and P. B. Bobba, "Extensive analysis on load dynamics of an unmanned aerial vehicle," in *2019 IEEE 5th International Conference for Convergence in Technology (I2CT)*, 2019, pp. 1–6.
- [27] S. Chen, Y. Li, and W. Dong, "High-performance relative localization based on key-node seeking considering aerial drags using range and odometry measurements," *IEEE Transactions on Industrial Electronics*, vol. 71, no. 6, pp. 6021–6031, 2024.
- [28] A. Shastry and D. A. Paley, "Uav state and parameter estimation in wind using calibration trajectories optimized for observability," *IEEE Control Systems Letters*, vol. 5, no. 5, pp. 1801–1806, 2021.
- [29] C. Böhm and S. Weiss, "Fuse-d: Framework for uav system-parameter estimation with disturbance detection," in *2023 IEEE/RSJ International Conference on Intelligent Robots and Systems (IROS)*, 2023, pp. 1774–1781.
- [30] J. Svacha, J. Paulos, G. Loianno, and V. Kumar, "Imu-based inertia estimation for a quadrotor using newton-euler dynamics," *IEEE Robotics and Automation Letters*, vol. 5, no. 3, pp. 3861–3867, 2020.
- [31] A. Gelman, J. Carlin, H. Stern, D. Dunson, A. Vehtari, and D. Rubin, *Bayesian Data Analysis, Third Edition*, ser. Chapman & Hall/CRC Texts in Statistical Science. Taylor & Francis, 2013. [Online]. Available: <https://books.google.com.hk/books?id=ZXL6AQAQBAJ>
- [32] W. Dong, Z. Mei, Y. Ying, S. Chen, Y. ie, and X. Zhu, "Sribo: An efficient and resilient single-range and inertia based odometry for flying robots," 2022. [Online]. Available: <https://arxiv.org/abs/2211.03093>



Kaiwen Xiong is currently pursuing the undergraduate degree in automation at Shanghai Jiao Tong University, Shanghai, China.

He is currently with the State Key Laboratory of Mechanical System and Vibration, School of Mechanical Engineering. His research interests include state estimation and adaptive positioning of unmanned systems.



Sijia Chen received the B.S. degree in mechanical design manufacture and automation from the University of Electronic Science and Technology of China, Sichuan, China, in 2022. She is currently a Ph.D. candidate with the State Key Laboratory of Mechanical System and Vibration, School of Mechanical Engineering, Shanghai Jiao Tong University.

Her research interests include state estimation and intelligent control of unmanned systems.



Wei Dong received the B.S. degree and Ph.D. degree in mechanical engineering from Shanghai Jiao Tong University, Shanghai, China, in 2009 and 2015, respectively.

He is currently an associate professor in the Robotic Institute, School of Mechanical Engineering, Shanghai Jiao Tong University. For years, his research group was champions in several national-wide autonomous navigation competitions of unmanned aerial vehicles in China.

In 2022, he was selected into the Shanghai Rising-Star Program for distinguished young scientists. His research interests include cooperation, perception and agile control of unmanned systems.